Investigating the Impact of Saharan Dust Aerosols on Analyses and Forecasts of African Easterly Waves by Constraining Aerosol Effects in Radiance Data Assimilation

By

Dustin F. P. Grogan[1]

Cheng-Hsuan Lu[1,2]

Shih-Wei Wei[1,2]

Sheng-Po Chen[1,3]

1. University at Albany, State University of New York, Albany, NY
2. Joint Center for Satellite Data Assimilation, Boulder, CO
3. Department of Chemistry, National Central University, Taoyuan, Taiwan

Submitted to

Atmospheric Chemistry and Physics

on

February 15th, 2021

Revised on

October 13th, 2021

Corresponding author: Dustin Grogan, University at Albany, 1400 Washington Ave, Albany, NY 12222; dgrogan@albany.edu

Formatted: Header

Formatted: Font: Not Bold, Font color: Black

Formatted: Centered

Deleted: Effects

Formatted: Indent: First line: 0"

Formatted: Font color: Black

Deleted: : The Impact of

Formatted: Font color: Black

Deleted: -Affected Satellite Radiances on

Formatted: Font color: Black

Formatted: Font color: Black

Deleted: .

Deleted: July 21st

Deleted: ¶

Formatted: Left, Indent: First line: 0"

Formatted: Font color: Auto

Formatted: Justified, Indent: First line: 0"

Abstract:

This study incorporates aerosol effects into satellite radiance calculations within the Global Data Assimilation System (GDAS) to investigate its impact on the analyses and forecasts of African easterly waves (AEWs). A comparison of analysis fields from the aerosol-aware assimilation experiment and an aerosol-blind control during August 2017 resulted in a warmer Saharan boundary layer; a faster African easterly jet; and AEWs with enhanced northern tracks and reduced southern tracks. The changes to the tracks are qualitatively consistent with arguments of baroclinic and barotropic instability. During the time period, we examined two AEWs that developed Hurricane Gert (2017) and Harvey (2017) over the Atlantic, but were structurally different over Africa; the AEW for Gert consisted of a southern circulation, while the AEW for Harvey consisted of a northern and southern circulation. Analysis differences of the cases showed stronger vorticity changes for the AEW that developed Harvey, which we attribute to the aerosol-aware assimilation capturing dust radiative effects involving a large-scale Saharan dust plume that interacted with the AEW's northern circulation. Forecasts from the Global Forecast System (GFS, v14) initialized by the different GDAS analyses for the AEW cases showed that the aerosol-aware experiment reduced errors in the downstream vorticity for the AEW that developed Harvey; neutral improvement was found for the AEW that develop Gert. Thus, aerosol-affected radiances in the assimilation system have the ability to correct analysis fields to account for the dust radiative effects on AEWs, which in turn can improve forecasts of the AEWs as they travel downstream.

1. Introduction

Formatted: Header
Deleted: time-varying aerosols
Formatted: Font color: Text 1
Deleted:) and their environment. Comparison
Deleted: showed that the aerosol-affected radiances accelerated the African easterly jet and West African monsoon flow; warmed the
Deleted: and modified the AEW vorticity structure,
Deleted: increases in the
Deleted: circulation
Deleted: decreases in the
Deleted: circulation. Analysis fields from each experiment were used in
Deleted: Global Forecast System (GFS) to examine differences in forecasting
Deleted: AEW cases
Deleted: hurricanes
Deleted: North
Deleted: . The aerosol-aware experiment reduced errors in forecasting
Formatted: Font color: Text 1
Deleted: case whose northern circulation interacted with
Formatted: Font color: Text 1
Formatted: Font color: Text 1
Deleted: other AEW, which did not contain a northern circulation nor interacted with a dust plume. ¶ The changes to the
Deleted: by
Deleted: aerosol-aware assimilation are reminiscent of
Deleted: that operate
Deleted: and their environment. That is, the aerosol-affected radiances produce corrections to the brightness temperatures that modify the analysis fields like dust aerosols that are radiatively coupled to the atmospheric variables in the forecast model. We show qualitatively that dust radiative effects are captured by the aerosol-affected radiances for the AEW case that interacted with a dust plume
Formatted: Font color: Black
Deleted: served to
Formatted: Font color: Black
Deleted: wave
Deleted:
Formatted: Font color: Auto

In regions around the world, aerosols can have a profound impact on weather. This is especially the case over North Africa as it houses the Saharan Desert, which is the largest emitter of mineral dust aerosols, and African Easterly Waves (AEWs), which are synoptic-scale circulation systems.

AEWs are the dominant synoptic-scale disturbance over North Africa from March to October (Carlson 1969; Burpee 1972). The waves develop along the African easterly jet (AEJ), which is a tropospheric jet (~650 hPa) whose axis is centered in the Sahel (~15°N). The AEWs are also maintained by the AEJ through barotropic and baroclinic energy conversions. (Norquist et al. 1977). Consequently, the AEWs can have two cyclonic circulations that reside on either side of the AEJ axis (Reed et al. 1988; Pytharilous and Thorncroft 1999). The circulation south of the AEJ peaks at ~650 hPa and is frequently coupled to moist convection (Kiladis et al. 2006; Berry and Thorncroft 2005), while the northern circulation peaks at ~850 hPa, is dry, and can be immersed in Saharan dust (Knippertz and Todd 2010; Grogan and Thorncroft 2019). Over the East Atlantic, the two circulation centers often merge into a single circulation, which can produce a favorable environment for tropical cyclogenesis (Schwendike and Jones 2010; Ross and Krishnamurti 2007).

During summer, Saharan dust emissions are most active over the western Sahel (16°N-24°N, 0°-15°W) (Cowie et al. 2014), the same region the AEW northern track resides. The emissions are driven by enhanced surface winds that blow over dry and erodible regions (Tegan and Fun 1994; Webb and Strong 2011). Once lifted, the dust mixes within the deep Saharan boundary layer (Cuesta et al. 2009; Knippertz and Todd 2012) and can form plumes that span thousands of kilometers. The transport of these large-scale dust plumes has been connected to African easterly waves (Westphal et al. 1988; Jones et al. 2003; Knippertz and Todd 2010; Nathan et al. 2019; Grogan and Thorncroft 2019). The dust can also be carried westward over the Atlantic

Formatted: Header

Deleted: Despite contributing less than 1% of the total mass to the atmosphere

Deleted: and climate

Deleted: in aerosol-rich regions, such as

Deleted: home to

Deleted: loadings for

Deleted: in the world. On average, approximately 1000 Teragrams of dust are emitted from the Saharan Desert each year (Huneeus et al. 2011). The emissions are driven by enhanced surface winds over extremely dry and erodible regions (Knippertz and Todd 2012). Once emitted, the dust mixes within the deep Saharan boundary layer (up to 500 hPa) and can form plumes that span thousands of kilometers. ¶
In summer, Saharan dust plumes are transported westward toward the Atlantic by the African easterly jet (AEJ) and African easterly waves (

Deleted:). The AEJ is a mid-

Deleted: on the southern edge of the Saharan Desert

Deleted:), while AEWs are synoptic-scale waves that develop along the AEJ.

Deleted: , which

Deleted: .

Deleted: ,

Deleted: .

Deleted: Meanwhile the dust moves

within the Saharan air layer (SAL) (Karyampudi et al. 1999; Chen et al. 2010), which is an elevated layer of dry air that originates from the Saharan boundary layer.

Dust directly affects the scattering and absorption of incoming and outgoing radiation of the atmosphere, which produces heating rates that can influence AEWs through two distinct pathways (Bercos-Hickey et al. 2017). The first pathway is through the background (time-averaged) dust fields, which produce heating rates that modify the background temperature and wind fields (i.e., the AEJ), which in turn affects AEW structure and development (Jones et al 2004; Wilcox et al. 2010; Jury and Santiago 2010). The second pathway is through the formation of large-scale episodic dust plumes, which produces heating rates that correlate with the wind and temperature of the AEW to directly affect its growth rates, phase speeds, energetics, and spatial structures (Grogan et al. 2016, 2017, 2019; Nathan et al. 2017).

To incorporate the above-mentioned dust radiative effects on AEWs within a numerical weather prediction (NWP) system, it is important to represent the episodic nature of the aerosols. These radiative effects have been included into NWP systems through two approaches: (i) radiatively coupling aerosols in the forecast model, and (ii) incorporating aerosols in satellite radiance calculations during data assimilation (DA).

For the first approach, aerosol attenuation modifies the heating rates within the radiation schemes of the forecast model of the NWP system. Studies have shown that this improves the forecast skill of several features in dust-affected regions over North Africa and the East Atlantic, including sea-level pressure and atmospheric temperature (Perez et al. 2006; Mulcahy et al. 2014), AEWs linked to tropical cyclogenesis (Reale et al. 2009; Reale et al. 2011; Chen et al. 2015), and the AEJ (Reale et al. 2014). Major efforts are also ongoing to improve aerosol prediction models, including the particle's emission and removal processes, assimilating observations such as aerosol

Formatted: Header

Deleted: The dust-laden SAL can infiltrate the AEW's oceanic circulation, which suppresses convection and thus tropical cyclone development (Dunion and Velden 2004; Reale et al. 2009; Braun et al. 2016; Brammer et al. 2018).

Formatted: Font color: Auto

Deleted: AEWs through changes in

Deleted: the

Deleted: . This

Deleted: dust-induced

Deleted: average (in

Deleted: or space

Deleted: ambient

Deleted:) that

Deleted: the

Deleted: when correlated

Deleted: wave can

Deleted: several AEW properties, including

Deleted: into

Deleted: realistic

Deleted: Studies have done this by including prognostic aerosol fields

Deleted: which has

Deleted: to improve

Deleted: affect

Deleted: , such as

Deleted: (e.g.,

Deleted: Mulcahey

Deleted: ;

optical depth (AOD), and model verification and evaluation (see Benedetti et al. (2018) for a comprehensive discussion). Such advances in aerosol prediction models can, in turn, improve weather prediction. But despite these advances, the radiatively coupling of episodic aerosols in the NWP system is often not feasible in an operational setting due to computational costs. Thus, most operational NWP systems use prescribed aerosol climatologies, such as the NCEP operational Global Forecast System (GFS; Hou et al. 2002) and the ECMWF integrated forecast system (IFS; Bozzo et al. 2017). Consequently, the NWP system sacrifices the ability to represent episodic aerosol signals.

For the second approach, aerosol transmittance effects are considered during radiance DA, which modifies the analysis fields of the NWP system. Kim et al. (2018) demonstrated this approach by including 3-hourly aerosol fields from the Goddard Chemistry Aerosol Radiation and Transport (GOCART) model into the radiance calculations within the Goddard Earth Observing System (GEOS)-atmospheric data assimilation system (ADAS). Kim et al. (2018) showed that when aerosols were considered, they found the fit to observations improved for satellite infrared (IR) sounders due to accounting for the aerosol transmittance effects in the form of cooling brightness temperatures (BT), which has been observed in previous studies (e.g., Sokolik 2002). As a result, the cooling of BTs led to warmer analyzed surface temperatures in the Tropical Atlantic. Similarly, Wei et al. (2020, 2021) showed that considering aerosol transmittance effects warmed analyzed sea-surface temperatures and low-level air temperatures over the transatlantic region and Africa when including aerosols from NOAA's Environmental Modeling System (NEMS) GFS Aerosol Component (NGAC) into NCEP's global data assimilation system (GDAS). Wei et al. (2020) also showed that the aerosols improved forecasting of vector winds and geopotential heights at multiple levels in the tropical region from the GFS model.

Formatted: Header

Deleted: simulating prognostic aerosols

Deleted: the

Deleted: Few other studies have incorporated aerosols into

Deleted: through the data assimilation system. For example,

Deleted: included

Moved (insertion) [1]

Deleted: They

Deleted: from

Deleted: improved by

Deleted: cooling effect

Deleted: documented

Deleted:

Moved up [1]: Kim et al.

Deleted: (2018) showed that

Deleted: aerosol

Deleted: on the BT

Deleted: heating of the

Deleted: temperature

Deleted: ¶
Similar to Kim et al. (2018),

Deleted: included

Deleted: the NOAA

Deleted: As a result, they found warmer analyzed sea surface temperatures in the Atlantic and warmer low-level analyzed air temperatures over Africa and the transatlantic region.

Deleted: the

Deleted: . Most operational NWP systems, however, ignore this process despite its relatively low computational cost

Formatted: Font color: Auto

Incorporating aerosol transmittance effects into the radiance calculation of DA is excluded from all NWP centers, despite its relatively low computation costs and its potential to leverage aerosol-affected radiances in a physical and consistent way. But more studies investigating this approach are needed. For example, no study has used this approach to examine the impacts of dust radiative effects on AEWs in the NWP system. Motivated by the results in Kim et. al. (2018) and Wei et al. (2020, 2021), along with the physical understanding of dust radiative effects on AEWs identified in the literature, this study seeks to examine how, and to what extent, episodic aerosols in the satellite radiance calculations can affect analyses and forecasts of AEWs over North Africa and the East Atlantic. We focus our analysis on two AEWs during August 2017 that are structurally different over North Africa but later developed hurricanes over the Atlantic.

In Section 2, we describe the model experiments and the methods used to track the AEWs. Section 3 presents the analysis differences and forecast performances from each experiment and examines the analysis results from the aerosol-aware experiment in the context of dust radiative effects on AEWs. Section 4 provides conclusions and a short discussion.

2. Experiments and Methods

2.1 Model Experiments

The schematic in Fig. 1 illustrates the workflow of the experiments in this study, which were conducted from July 25th – August 28th, 2017. The first experiment is an aerosol blind run (CTL), where aerosols are not considered in the assimilation system. The second experiment is an aerosol-aware run (AER), which constrains aerosol transmittance effects into the radiance calculations of the assimilation system (i.e., aerosol-affected radiances). For our experiments, we employ version 14 of the National Centers for Environmental Prediction (NCEP) Global Forecast System (GFS, v14), which consists of an analysis system, the Global Data Assimilation System

Formatted: Header

Formatted: Font color: Text 1

Deleted:) and

Deleted: impacts

Deleted: examines

Deleted: of the data assimilation system

Deleted: the atmosphere

Deleted: . Section 4 discusses

Deleted: of

Deleted: and its relationship to

Deleted: AEW within the analysis fields.

Deleted: 5

Deleted: concluding remarks

Formatted: Font color: Text 1

Deleted:

Formatted: Font color: Text 1

Deleted: To investigate the impact of incorporating aerosols into the assimilation of satellite radiances, this study employs version 14 (v14) of NCEP's GFS forecast model and the corresponding GDAS. Briefly, the GFS v14 is a global spectral model that accounts for aerosol direct radiative effects using prescribed monthly aerosol climatologies from the Optical Properties of Atmospheric Composition (OPAC) software package (Hess et al. 1998). Meanwhile, the GDAS is a Gridpoint Statistical Interpolation (GSI) based four-dimensional ensemble-variational (4DEnVar) assimilation system that excludes any explicit treatment of aerosols. For our study, the NWP system is run at coarser resolution than NCEP's operational settings: we use T670 (~30km) resolution for the GFS forecast model and 80 ensemble members running at T254 (~80km) resolution for GDAS. ¶

Formatted: Font color: Text 1

Deleted: each experiment

Formatted: Font color: Text 1

Deleted: . Two experiments

Formatted: Font color: Text 1

Deleted: , spanning

Formatted: Font color: Text 1

Deleted: the aerosol effects on radiance

Formatted: Font color: Text 1

Deleted: GDAS (as is by default).

Formatted: Font color: Text 1

Deleted: incorporates time-varying

Formatted: Font color: Text 1

Deleted: information

Formatted: Font color: Text 1

Deleted: within GDAS. Both cases

(GDAS), and a forecast model, the global spectral model (GSM), with GFS physics. The experiments are fully-cycled, which means that each analysis is constructed from their respective forecasts of the prior cycle.

The analyses are constructed using GDAS (Fig. 1: blue), which is a Gridpoint Statistical Interpolation (GSI) based four-dimensional ensemble-variational (4DEnVar) assimilation system. The assimilation system is run for 80 ensemble members at T254 (~80km) resolution. In GDAS, the radiance calculations are conducted by the Community Radiance Transfer Model (CRTM) (Lu et al. 2021). The CRTM generates simulated brightness temperatures (BT) and computes the radiance sensitivities with respect to the state variables (Han et al. 2006).

For both experiments, various observations are ingested into GDAS, including the conventional dataset (e.g., radiosondes, ships, buoys, etc.), and satellite observations (e.g., retrievals and radiances) (Fig. 1: gray). In particular, for the radiance observations, we include the level 1 product of IR and microwave sensors, which are pre-processed by NOAA's National Environmental Satellite, Data, and Information Service (NESDIS). For a complete list of the thermal IR sensors, see Table 1 of Wei et al. (2021).

For AER, aerosol transmittance effects can be constrained in CRTM by ingesting three-dimensional aerosol mixing ratios into GDAS. CRTM contains look-up tables for aerosol optical properties—absorption coefficient, single scattering albedo, and asymmetric factor— to compute the aerosol affected radiances (Lu et al. 2021). The optical properties are based on the Optical Properties of Atmospheric Composition (OPAC) software package (Hess et al. 1998).

The aerosol mixing ratios are provided by the NEMS GFS Aerosol Component model (NGAC, v2) (Fig. 1: gold), which is based on GOCART (Colarco et al. 2010). NGAC simulates the emission, mixing, transport and removal (wet and dry) for 15 externally mixed aerosols,

Formatted: Header

Formatted: Font color: Text 1

Deleted: runs, meaning

Formatted: Font color: Text 1

Deleted: 6-hour

Formatted: Font color: Text 1

Deleted: using

Formatted: Font color: Text 1

Deleted: from

Formatted: Font color: Text 1

Deleted: of the respective experiment.

Formatted: Font color: Text 1

Deleted: To enable the aerosol-aware option in AER, mixing ratios of dust, sea-salt, sulfate, organic carbon and black carbon aerosols from the NGAC, v2 model (Wang et al. 2018) are ingested into GDAS and passed to the Community Radiative

Formatted: Font color: Text 1

Deleted: , v2.2.4), which is the radiance observation operator in GSI. Briefly, the

Formatted: Font color: Text 1

Deleted: contains a fast-forward radiative model, which

Formatted: Font color: Text 1

Deleted: BTs for the observations in the same space-time domain, and also contains Tangent-Linear, Adjoint, and K-Matrix models, which together compute the

Formatted: Font color: Text 1

Deleted: More details on the implementation of aerosols in GDAS can be found in Wei et al. (2021), which uses the same methodology as this study.

Formatted: Font color: Text 1

Deleted: In addition to the fully cycled analyses, we also produced 34 consecutive GFS forecasts for CTL and AER during the period of interest (July 25th-August 28th). Each forecast was initialized at 00Z of the respective analysis and ran for 120 hours. Despite having differences in the GDAS configuration, both experiments use the same forecast model (i.e., the GFS v14), which is radiatively coupled to prescribed OPAC aerosol climatologies. This means that differences between the two sets of forecasts arise solely by the initial conditions via the incorporation of aerosols in the GDAS radiance calculations, rather than adjustments to the physics within the GFS forecast model.

Formatted: Header

including dust, sea salt, sulfate, organic carbon, and black carbon. (Lu et al. 2016; Wang et al., 2018). The NGAC forecasts are used to predict the aerosols mixing ratios during the analysis window of each cycle. Like the meteorological fields, the aerosol mixing ratios are interpolated to the observations in space and time using the First Guess at Appropriate Time (FGAT) (Lorenc and Rawlins 2005). Figure 2 shows the NGAC forecasts total AOD (all aerosols at 550nm) averaged over August 1-28th, 2017. The AOD peaks over the Western Sahara, near the coast of West Africa, and in the Bodéléle Depression, within the interior of the continent, which are consistent with source regions over summertime in North Africa (Engelstader and Washington, 2007). The AOD, however, overestimates the hotspots by ~25% when compared to the summer AOD climatology from the Modern-Era Retrospective analysis for Research and applications (MERRA, v2) (Randles et al. 2016). Nonetheless, the use of NGAC does not affect our qualitative interpretation of the aerosol-affected radiances on the analyses and forecasts.

We also conducted short-range forecasts in each experiments' fully cycled system. To do this, the forecast model within GFS is used to run 120-hr weather forecasts at T670 (~30km) resolution, which are initialized on 00 UTC of each day (Fig. 1: green). The forecast model does account for aerosol radiative effects using prescribed monthly aerosol climatologies from OPAC (Hess et al. 1998). But for both experiments, we use the *same* configuration in the forecast model, which means that changes to the forecasts arise solely by the model's response to the analysis differences, rather than the physics driving the forecast model.

To demonstrate the aerosol impact on the IR radiances, Fig. 3 shows a timeseries of each experiment's observation-minus-forecast (OMF) BT for an IR channel (12.93 um) from the Infrared Atmospheric Sounding Interferometer (IASI); the channel and sensor are representative for other IR window channels and thermal IR sensors, respectively. For both experiments, the

OMFs, which are averaged over North Africa and the East Atlantic, have a similar root-mean-square (RMS) (Fig. 3a) and negative, or cold, bias (Fig. 3b) during the period of interest. But for the cold bias, the AER run (red) is slightly more positive than the CTL run (blue). This difference is due to the incorporation of aerosol transmittance effects on the forecast (simulated) BT (via scattering), which in turn reduces the cold bias in the OMFs. The average impacts are small (~1.7K) over the region, but the bias differences can be substantial (up to ~10K) in localized regions during strong Saharan dust events (Sokolik et al. 2001). When the aerosol-affected OMFs are assimilated, this produces warmer analyzed temperatures at low-levels in the atmosphere (Weaver et al. 2003; Kim et al. 2018; Wei et al. 2021).

2.2 Wave tracking

To identify the synoptic wave patterns during the period of interest, we used an objective tracking algorithm similar to that in Brammer and Thorncroft (2015). Briefly, the tracking algorithm involves analyzing mass-weighted centers of vorticity at multiple levels (i.e., curvature vorticity at 850, 700, and 500 hPa; relative vorticity at 850 and 700 hPa). The wave center is then determined from a weighted average of the centers within a specified radius (500 km). For each experiment, the wave centers were extracted using the 6-hourly analysis fields, which identified several systems that traversed North Africa and the East Atlantic. The tracking included waves that later developed hurricanes, which we focus on in this study given their long lifetimes and downstream implications.

For our time period of interest, two hurricanes developed from AEWs: Gert (2017) and Harvey (2017). Figure 4 shows the objective track locations for the AEWs that developed Hurricane Gert and Harvey in the CTL run over North Africa and the East Atlantic. For Gert (solid line), the storm originates over Northeast Africa, at 5 – 10°N, on July 31st and moves

Formatted: Header

Formatted: Font: Not Italic, Font color: Text 1

Deleted: east

Deleted: This

Deleted: 2

Deleted: hurricane

Deleted: (blue) and AER (red)

Deleted: Fig. 2a), the tracks show that northwestward over North Africa and reaches the East Atlantic on August 4th. In contrast, Harvey (dotted line) originates from two circulations over North Africa, at 25 – 29°N and 8 – 12°N, that develop on August 8th and merge into one circulation near the coast, on August 12th; the storm then moves west/southwest over the East Atlantic. Both waves then developed hurricanes while over the western portion of the Atlantic Ocean.

Comparison of the track locations for CTL and AER show little difference in the storm positions during their evolution (not shown). After the initial development, the track locations among the two cases are less than 250 km. Given the wavelength of the AEWs span 2000 – 5000 km (Burpee 1974), the aerosol-aware assimilation does not appear to have a significant influence on the wave tracks. Therefore, we use track locations from CTL when investigating the storm structures in the analyses and forecasts for both cases.

3. Results

3.1 Analysis Differences: Time-average fields

Before investigating the AEW cases shown in Fig. 4, we first examine the aerosol impacts on the time-averaged background temperature, background zonal wind, and AEW meridional wind variances.

Figure 5 shows cross-sections of the time-averaged background temperature and zonal wind for CTL (contours) and the AER – CTL difference (colors) averaged over August 1st-28th, 2017. Consider first the CTL run. The experiment captures the main summertime circulation features over the region. For temperatures, the warmest air is positioned near the surface over the Saharan Desert (Fig 5a: 20°N-30°N). This warming sets up a strong meridional temperature gradient that extends vertically up to ~650 hPa and horizontally across the Sahel and over the East Atlantic (Fig. 5b: 30°W-20°E). For the zonal wind, there is a well-defined AEJ at 650 hPa (Fig.

Formatted: Header

Deleted: .

Deleted: Fig. 2b

Deleted: which

Deleted: that

Deleted: over North Africa and the East Atlantic.

Deleted: to investigate

Deleted: in the next section

Deleted: 2

Deleted: fields that the waves propagate through. Figure 3 shows cross-sections of the

Deleted: temperature for CTL (contours) and the AER – CTL difference (colors) averaged over August 2017

Deleted: , including the

5c: 15°N) that extends across North Africa and the East Atlantic (Fig. 5d: 20°W – 15°E, 10°N – 15°N) and low-level westerlies (800-1000 hPa) that are associated with the West African Monsoon (WAM) flow (Fig 5c: 8°N-18°N).

The AER – CTL differences in Fig. 5 indicate how the aerosol-affected radiances impact the time-averaged background fields. For temperature, the aerosol impacts warm the Sahara and Sahel in the boundary layer by ~0.5 K (reddish colors in Fig. 5a: 10°N – 30°N, 1000 hPa – 650 hPa) and cool the marine boundary layer below the SAL by ~0.5 K (blueish colors in Fig. 5b: 15°N – 25°W, 15°N – 30°N). These temperature changes are qualitatively consistent with enhanced aerosol heating in the boundary layer over the continent and in the SAL offshore. Over land, the heating peaks at 800 hPa in the Sahel and the southern Saharan Desert (Fig 5a: 15°N -25°N). The position of the heating means that the aerosol-aware assimilation (i) increases lapse rates (or reduced static stability) at low levels in the Sahel and southern Sahara (15°N – 25°N 1000 – 800 hPa) and (ii) enhances the meridional temperature gradient in the Sahel (Fig 5a: 12°N – 20°N, 1000-600 hPa; Fig 5b: 10°W-10°E, 12°N-20°N).

The AER – CTL differences in temperature support the changes to background zonal wind via adjustments to the thermal wind. For example, along the enhanced meridional temperature gradient (12°N-20°N), AER accelerates the AEJ by ~0.5 m/s (blueish colors in Fig. 5c: 10°N – 15°N, 700 – 600 hPa, and Fig. 5d: 20°E – 30°W, 10 – 15°N), and accelerates the westerly flow of the WAM by about ~1.0 m/s (reddish colors in Fig. 5c: 12°N – 19°N, 1000 – 850 hPa). Away from these features, the structural changes to the zonal wind are more difficult to interpret. But assessment of shear difference plots (not shown) show that the aerosol-aware assimilation: (i) increases the vertical shear below the AEJ (15°N – 22°N, 900 – 700 hPa) and (ii) decreases the horizontal shear on the flanks of the AEJ axis (8°N – 18°N, 800 – 600 hPa).

Formatted: Header

Deleted: 3a

Deleted: °

Deleted: , 600 hPa

Deleted: 3b

Deleted: 25°E, 10 –

Deleted: the

Deleted: . 3a: 1000 – 800 hPa). The CTL experiment also accurately positions the warmest air temperatures near the surface over the Saharan Desert, which consequently sets up a strong meridional temperature gradient in the Sahel that drives the AEJ (Fig. 3c: 10 – 20°N, 1000 – 650 hPa; Fig. 3d: 15°W – 20°E, 10 – 15°N).

Formatted: Font color: Auto

Deleted: 3

Deleted: analysis

Deleted: For the zonal wind, the differences indicate that AER accelerates the AEJ core by ~0.5 m/s across North Africa and the Eastern Atlantic (blues in Fig. 3a: 14 – 16°N, 700 – 600 hPa, and Fig. 3b: 20°E – 30°W, 10 – 15°N), accelerates the WAM flow by ~0.5 m/s (reds in Fig. 3a: 12 – 22°N, 1000 – 800 hPa), and accelerates the easterly flow by ~0-2-0.5 m/s south of the AEJ axis (blues in Fig. 3a: 12 – 22°N, 1000 – 600 hPa). The accelerated flows infer a structural change in the AEJ, including intensifying the low-level vertical shear north of the AEJ core (15 – 22°N, 900 – 700 hPa) and weakening the mid-level horizontal shear south of the AEJ axis (8 – 12°N, 800 – 600 hPa).
For AER – CTL difference in ambient

Formatted: Font color: Black

Deleted: (reds

Deleted: 3c

Deleted: – 500

Deleted: (blues

Deleted: 3d

Deleted: Over the Sahara, the heating peaks at 800 hPa, which in turn, infers a region of reduced static stability below the peak heating (15 – 25°N, 1000 – 800 hPa).

Deleted: The temperature changes also support

Formatted: Font color: Text 1

Deleted: corresponding zonal wind changes via thermal wind. For example, the additional warming in

Deleted: boundary layer will enhance

Deleted: 10

Deleted:). This increases the vertical shear at low- and mid- levels (1000-500 hPa), driving accelerations in the WAM below and AEJ above.

Formatted: Font color: Text 1

Deleted: Changes to the AEJ and temperature can affect the structure and development of AEWs. Therefore, we next examine the AEW activity over the time period. To do this, Fig. 4 shows time-averaged cross-sections of the relative vorticity amplitude modulus; this quantity is a proxy for AEW activity but has limitations as it includes the cyclonic and anticyclonic vorticity from all scales in its computation. ... [1]

Figure 6 shows a vertical cross-section of the time-averaged, 2-6 day filtered meridional wind variance, a proxy used to assess AEW amplitudes (Reed et al. 1988; Pytharilous and Thorncroft 1999). The filtered meridional wind variances capture the two AEW tracks over the interior of North Africa (contours show the CTL run). For both experiments, the wave structures peak at levels consistent with AEWs examined in previous studies (southern: 8°N – 13°N, 700 – 600; northern: 18°N – 22°N, 950 – 800 hPa). But the AER – CTL differences (colors) show that for the AER run, the meridional wind variances increase by ~15% in the northern circulation and decrease by ~10% in the southern circulation. Note that the AER run also increases the wind variances near the AEJ core by ~25% (15°N, 600 hPa), but this increase does not change the peak location of the southern circulation.

The differences in the AEW meridional wind variances shown in Fig. 6 are, in part, due to changes to the background fields, which can be explained by the local wave energetics (Norquist et al. 1977; Hseih and Cook 2005; Bercos-Hickey et al. 2020). In absent of diabatic processes, the AEW's southern structure extracts energy from the background via barotropic conversions, which are proportional to the horizontal shear of the AEJ, while the northern structure extracts energy via baroclinic energy conversions, which are inversely proportional to the static stability (Thorncroft and Hoskins 1994; Paradis et al. 1995; Thorncroft 1995). This means that for AER, the changes to the background zonal wind and temperature (i) reduce wind variances in the southern circulation via decreased horizontal shear on the equatorward side of the AEJ (barotropic) and (ii) increase wind variances in the northern circulation via reduced static stability below the AEJ (baroclinic).

The qualitative explanation of how aerosol-affected radiances impact the waves via the background fields aligns with the first of two pathways in which dust can affect AEWs mentioned in the introduction. For AER, the aerosol-aware assimilation captures dust radiative effects that

Formatted: Header
Deleted: . The
Formatted: Font color: Text 1
Deleted: 800
Deleted: 700
Deleted: Moreover,
Deleted: AER modified
Deleted: two tracks by increasing vorticity
Deleted: (800-1000 hPa)
Deleted: decreasing it
Deleted: (700-900
Deleted:). To determine if these
Moved (insertion) [2]
Formatted: Font color: Black
Deleted: are associated
Formatted: Normal (Web), Justified, Indent: First line: 0.5", Line spacing: Double
Formatted: Font color: Black
Formatted: Font color: Black
Deleted: , we next

operate on the analyzed background temperature, AEJ, and thus the AEW wind variances. But it's worth mentioning that dust radiative effects are coupled to the forecast model (i.e., from the OPAC aerosol climatology), which also operate on the analysis fields via the first-guess meteorological fields. Thus in AER, changes to the time-averaged fields in Figs. 5 and 6 are due to the time-averaged NGAC aerosols in the assimilation system modifying existing radiative effects imposed by the OPAC aerosol climatology in the forecast model. To investigate the impact of episodic dust plumes in the assimilation, we turn next to our AEW cases.

3.2 Analysis Differences: AEW cases

Figure 7 compares the structure of the AEW that developed Gert for CTL and AER. The AEW crosses Africa and the East Atlantic from July 31^{st} to August 4^{th}. During these times, the wave remains south of the AEJ and is thus largely away from the dust aerosols. But despite this separation, the aerosol-aware assimilation affects the evolution of the wave structure (Fig 7a, 7c: colors surrounding the X's). For example, on Aug 2^{nd}, the AER run decreases the wave, which is an open trough (Fig 7a: blueish colors surrounding the X). The vertical structure also shows that the vorticity for AER (red) is ~10% less than the for CTL (blue) from 600 – 800 hPa (Fig. 7b). On Aug 4^{th}, the wave intensifies as it moves offshore, forming a closed streamline circulation (Fig. 7c). But similar to the onshore wave, the aerosol impacts on the vertical structures continue to reduce the cyclonic vorticity within the storm center by ~10% (Fig. 7d).

Figure 8 compares the structure of the AEW that developed Harvey for CTL and AER. The AEW develops as two circulations over East Africa on August 8^{th} and travels west. On August 9^{th} the land-based AEW is broad in structure and covers a large portion of the continent (Fig. 8a). For AER, there are strong changes within both circulation centers, which include increases in the vorticity around the northern circulation structure (reddish colors at 18°N) and decreases in the

Formatted: Header

Formatted: Font color: Black

Formatted: Font color: Black

Deleted: identified in section 2

Formatted: Font color: Black

Formatted: Font color: Black

Deleted: Figures 5-8 shows

Deleted: horizontal and vertical structures of the AEW cases as they transverse across North Africa. The horizontal structures in Figs. 5 and 7 respectively show the 700 hPa and 850 hPa CTL streamlines (contours) and the AER – CTL differences in the cyclonic vorticity at the level of the streamlines (colors); the wave centers are denoted by X's. Figures 6 and 8 show the corresponding vertical

Deleted: vorticity, circular averaged around the wave centers (radius 500 km). Because the AEW that developed Harvey has two circulations, Fig. 8 shows the vertical structures of the northern and southern wave centers for Aug 9^{th} – 10^{th}, which are the times when the AEW amplitudes were largest over Africa ¶
For the

Deleted: , Fig. 5 shows the wave structure is confined

Deleted: (i.e., south of 15°N) as it crosses North Africa. This region is

Deleted: aerosol-free during

Deleted: time of year, but

Deleted: still clearly

Deleted: and 3^{rd}, Figs. 5b and 5c show

Deleted: cyclonic vorticity (blues

Deleted: X's). Looking at the average

Deleted: of the AEW vorticity, Fig. 6

Deleted: amplitudes

Deleted: are as much as 20% larger than AER (red)

Deleted: . Thus, the reduced vorticity in AER for this case is consistent with the time-averaged vorticity moduli shown for the AEW southern track

Deleted: 4).

Deleted: For

Deleted: , Fig. 7 shows that the wave has

Deleted: prominent cyclonic

Deleted: and a

Deleted: that

Deleted: North Africa. The AER run produces

Deleted: to

Deleted: increasing

Deleted: reds

Deleted: decreasing

southern circulation (blueish colors at 14°N). The vertical structures show that vorticity for the northern circulation is, on average, ~20 – 35% larger from 600-850 hPa (Figs. 8b: cf. solid blue and solid red), while the southern circulation is ~20 – 35% smaller from 750-850 hPa (Figs. 8b: cf. dotted blue and dotted red). On August 12th, the two circulations merge into a single wave offshore. Compared to the land-based AEW, the amplitudes of the combined wave are weak and its vertical structure changes little with height (Fig 8c, 8d). Consequently, the aerosol impacts are reduced, affecting the vorticity by ~5-15% from 1000-500 hPa (Fig. 8d).

Over Africa, the aerosol impacts on the AEWs for Gert and Harvey were consistent with the time-averaged AEW meridional wind variances in Fig. 6, but the impacts were stronger for Harvey. The story is different offshore: the impacts remain moderate for Gert but weaken for Harvey; the latter may be due to the merging of the circulations and the positioning of the aerosols. Therefore, we focus on land-based AEWs and further investigate the aerosol impacts.

To understand how the aerosol-aware assimilation impacts our AEW cases, it is informative to examine the episodic dust plumes and radiance observations as the waves crosses West Africa. Thus, Fig. 9 shows a snapshot of the NGAC AOD (brown contours) for times when the AEW for Gert (a) and Harvey (b) are over Africa; the X's mark the position of the circulation centers. Overlaying the AOD are observations from the IASI sensor at the same time; shown are the AER – CTL differences in the BT at 12.93μm (circles), the same sensor and channel shown in Fig 3. For Gert, the BT differences surrounding the wave center are negative. This indicates that near the wave center, the BTs are cooler in the AER run (Fig. 9a), but the values are small (light blue circles). In contrast, for Harvey, the negative values are large near the northern circulation (dark blue circles), which is also immersed in a dust plume with AODs over 1.0 (Fig. 9b).

Formatted: Header

Deleted: blues

Deleted: During August 9th and 10th, which are times when the AEW amplitudes are largest, Fig. 8 shows that the vorticity at 600-850 hPa

Deleted: for

Deleted: northern

Deleted: (Figs. 8a and 8c), and

Deleted: for the southern circulation (Figs. 8b and 8d). Therefore, the

Deleted: to the vorticity

Deleted: this case

Deleted: also consistent with those from the time-averaged vorticity moduli

Deleted: . 4. Moreover, the aerosol impacts on this AEW

Deleted: more intense than for

Formatted: Header

When aerosol-affected radiances are assimilated, warmer analyzed temperatures are produced at low-levels over North Africa and the East Atlantic (Kim et al. 2018; Wei et al. 2021). For the AEW that developed Gert, the warming over Africa is similar to the time-averaged AER-CTL background temperatures shown in Figs. 5a and 5b. For the AEW that developed Harvey in AER, however, the temperatures over the wave's northern circulation (18-22°N) warms as much as 1.5 K at mid-levels, 900-600 hPa, which is double the average. The implications of this additional warming on the AEW vorticity is explained below.

Grogan and Thorncroft (2019) showed through energetic arguments that the heating from an episodic dust signal that interacts with the AEW's northern circulation generates eddy available potential energy (APE ~ T'^2). Previous idealized studies have also shown that dust-induced eddy APE amplifies the northern structure of AEWs (Grogan et al. 2016, 2019; Nathan et al. 2017; Bercos-Hickey et al. 2017). For the Harvey case in the AER run, the scenario is the same as in Grogan and Thorncroft (2019), but the aerosol-affected radiances capture the heating from the dust plume, rather than the forecast model, which in turn drives the amplified vorticity in the AEW's northern circulation.

The qualitative explanation of how aerosol-affected radiances impact the AEW that developed Harvey via the episodic dust field aligns with the second pathway in which dust can affect AEWs mentioned in the introduction. Thus, the combined effects may help to explain why the aerosol impacts for the AEW with Harvey is stronger than the AEW with Gert.

Formatted: Font color: Black

3.3 *Forecast Differences: AEW cases*

To examine the impact of the aerosol-aware assimilation on the forecasts for our AEW cases, we compare the Root-Mean-Square-Error (RMSE) in vorticity for CTL and AER; the forecasts were verified against their respective analysis. Table 1 shows the RMSE relative

Deleted: compared

differences between AER and CTL for the 1000 – 500 hPa vorticity following the AEWs. To compute the RMSE following the AEW at each forecast time, we use the CTL wave locations shown in Section 2. For Gert, a 10° latitude by 10° longitude window is centered on the wave. For Harvey, our window over North Africa has a fixed latitude of 5 – 25°N and a 15° longitude range that is centered on the two circulations; over the Atlantic Ocean, a 10° latitude by 10° longitude window is centered on the merged circulation.

Table 1 shows the AER run produces neutral improvement in the forecasting of the AEW that developed Gert, as evidenced by the mixture of red and green values in the RMSE relative differences. Inspection of the forecasts show that both AER and CTL underestimate the intensification of the AEW when initialized onshore, on July 31st – Aug 2nd, and overestimate the intensification when initialized offshore, on Aug 3rd. As a result, there were several instances where the RMSE forecast differences did not produce statistically significant results (i.e., crossed out values for Gert in Table 1).

In contrast to the AEW that developed Gert, Table 1 shows the AER run produces statistically significant improvement in forecasting the AEW that developed Harvey. The largest improvements are found on the forecasts initialized on August 10th and 11th, with the forecast on August 10th showing reductions in RMSE on every forecast day (errors reduced by ~15-49%). For the initialized times that we examine for Harvey (Aug 8th -11th), both the analyzed amplitudes and AER – CTL vorticity differences were larger than Gert while onshore (cf. Figs. 6 and 8). Inspection of the forecasts reveal that the CTL run continues to suppress the wave amplitudes downstream, while the AER run better maintains the intensity of the wave as the two circulations merge over the East Atlantic and travel downstream.

Formatted: Header
Deleted: that developed Gert and Harvey.
Deleted: used
Deleted: was
Deleted: circulation
Deleted: had
Deleted: was
Deleted: was
Deleted: produced
Deleted: underestimated
Deleted: overestimated
Deleted: produced
Deleted: were
Deleted: examined
Deleted: revealed
Deleted: continued
Deleted: storm
Deleted: maintained
Deleted: storm
Deleted: merged
Deleted: traveled
Deleted:

In summary, the forecast error of the 1000-500 hPa averaged vorticity for the AEW that developed Gert are similar among the two experiments, but dramatically reduced in AER for the AEW that developed Harvey. This marked improvement with Harvey is likely associated with the aerosol-aware assimilation capturing radiative effects of the large-scale Saharan dust plume that interacted with the AEWs northern circulation. Therefore, ingesting mixing ratios of episodic aerosols to constrain radiance calculations within the assimilation system can improve forecasting the evolution of AEWs.

4. Conclusions and Discussion

In this study, we examined how incorporating time-varying aerosols into the assimilation of satellite radiances affected the analyses and forecasts using GFS v14 and the corresponding GDAS. In particular, we investigated the impacts of Saharan dust on the analyses and forecasts of AEWs and their environment over North Africa and the East Atlantic during August 2017. To do this, aerosol forecasts from the NGAC, v2 model were ingested into GDAS and constrained to the radiance calculations to produce analysis fields (aerosol-aware) that were compared to a control experiment that excluded aerosols (aerosol-blind). The analysis fields from both cases were then used to forecast two AEW cases during our time period that were structurally different over Africa, but later developed Hurricane Gert (2017) and Harvey (2017) over the Atlantic Ocean.

Analysis differences showed that the aerosol-aware assimilation affected several fields over North Africa and the East Atlantic. For example, the aerosols warmed the Saharan boundary layer, accelerated the AEJ and the westerlies associated with the WAM, and modified AEW meridional variances, with amplitudes increasing within the northern circulation and decreasing in the southern circulation. The changes in the AEW meridional variances were also consistent with the vorticity changes for the individual AEW cases examined.

Formatted: Header

Deleted: 4. Discussion

Deleted: this section, we discuss the relationship between the analysis differences shown in section 3.1 and 3.2 to the impacts of dust when aerosols are radiatively coupled to the forecast model, as well as the implications of the analysis differences on the forecasting of our AEW cases shown in section 3.3.
Consider first the time-averaged results in section 3.1. Analysis differences showed that the AER run accelerated the AEJ and WAM, and warmed the Saharan boundary layer. These changes, in turn, affect the structure of the wind shear and static stability that, in part, can explain the structural changes in the time-averaged vorticity amplitudes associated with the AEWs. This can be inferred from local wave energetics (Norquist et al. 1977; Grogan et al. 2019). For example, enhanced low-level vertical shear and reduced static stability setup below the AEJ core will increase local baroclinic energy conversions and thus vorticity in the north circulation. Additionally, reduced horizontal shear south of the AEJ axis will decrease local barotropic energy conversions in the southern circulation. Thus, the aerosol-aware assimilation modifies the existing dust radiative effects coupled to the forecast model (i.e., from the OPAC aerosol climatology) that operate on the analyzed AEJ, temperature, and AEW structures.
Consider next the analysis fields for the AEW cases examined in section 3.2. For the AEW that developed Gert, we found average values of aerosol optical depth (AOD) over the Sahara during the wave's passage over North Africa. In contrast, the AEW that developed Harvey interacted with a strong Saharan dust plume as it crossed North Africa. This can be seen in Figure 9, which shows a snapshot of the AOD (brown contours) surrounding the AEW northern circulation center (13.5°W, 20°N) on August 10th, at 12:00Z. Figure 9 also shows observations from the Infrared Atmospheric Sounding Interferometer (IASI) that were assimilated over the region at the same time; the observations are AER – CTL differences in the BT at 12.95μm (circles). Most of the differences ... [2]

Moved up [2]: 2020).

Formatted: Font color: Black

Formatted: Font color: Black

Deleted: ... [3]

Deleted: in

Deleted: dramatic reductions

Formatted: Font color: Black

Deleted: the forecast error

Formatted: Font color: Black

Deleted: the realistic representation

Deleted: , and its corresponding radiative effects on the AEW.

Deleted: this implies that the treatment

Deleted: of the NWP

Deleted: 5

Deleted: aerosol

Deleted: the

Deleted: vorticity structure

Deleted: These vorticity

Deleted: shown in

Deleted: , which were structurally different over North Africa but later developed into hurricanes over the West Atlantic

The impact of the analysis differences on forecasting the AEW cases was also examined. For the AEW that developed Gert, RMSE differences showed that the aerosol-aware experiment produced neutral improvement to the vorticity field among the forecasts tracking the wave over North Africa and the Atlantic. In contrast, the aerosol-aware experiment improved the vorticity field in most forecasts for the AEW that developed Harvey; the largest reductions in RMSE occurred when analysis differences in the AEW structures were largest.

In exploring the results, we showed qualitatively that the aerosol-aware experiment (via NGAC aerosols) captured the two pathways involving dust radiative effects on the AEWs that are mentioned in the introduction. For example, the aerosol-aware experiment modified the analyzed background temperature and AEJ, which in turn modified the analyzed time-averaged AEWs (the first pathway). Additionally, the aerosol-aware assimilation captured the enhanced warming and vorticity associated with the formation of an episodic plume interacting the northern circulation of the AEW that developed Harvey (second pathway). This response is similar for dust-coupled AEWs (Grogan and Thorncroft 2019). In contrast, this effect was absent for the AEW the developed Gert, which did not have a northern circulation nor interact with a dust plume.

The improvement on forecasting the AEW that developed Harvey suggests the importance of the aerosol-aware assimilation capturing dust radiative effects on AEWs involving episodic dust plumes. The AEW that developed Gert, however, was influenced by the radiative effects involving the time-averaged background fields, which were captured by the forecast model (via OPAC) and the aerosol-aware assimilation (via NGAC), did not improve forecasting the storm. Therefore, investigating more cases, both of which that interact with episodic dust plumes and those that do not, would better determine the utility of our approach for forecasting AEWs. Moreover, there are known variabilities in AEW activity (Brammer and Thorncroft 2017) and dust source regions over

Formatted: Header
Deleted: individual
Deleted: aerosols
Deleted: assimilation
Deleted: AEW structure
Deleted: associated with the time-varying aerosols
Deleted: radiance observation operator (i.e., CRTM).
Deleted: assimilation
Deleted: existing dust radiative effects operating on the
Deleted: AEJ and
Deleted: AEW vorticity structure.
Deleted: within
Deleted: enhanced warming and vorticity in the region, which is a similar
Deleted: shown previously
Deleted: e.g., Grogan et al. 2016;
Deleted: Consequently, the analysis changes significantly improved
Formatted: Font color: Black
Formatted: Font color: Black
Formatted: Font color: Black
Deleted: downstream. Forecast

West Africa (Wagner et al. 2016) that should also be examined. Nonetheless, forecast improvements such as those shown for the AEW that developed Harvey are encouraging and could be critical for determining the timing and location of tropical cyclogenesis that originate from developing AEWs.

Aerosol radiative effects can be incorporated into the NWP system through the forecast model and through the assimilation system. Though few studies focus on the assimilation approach, such as Kim et al. (2018) and Wei et al. (2021), this study has demonstrated the importance of incorporating time-varying, episodic aerosols into the satellite radiance calculations to capture dust radiative effects on the analyzed AEWs. More work, however, is needed to better understand how to optimize the aerosol-aware assimilation, such as adjusting the bias-correction and quality-control procedures (Wei et al. 2021). Moreover, future work should investigate how much complexity is needed to represent aerosol processes adequately and accurately, and thus effectively account for aerosol effects within the NWP system.

Data availability

Analyses and forecasts from the AER and CTL runs can be provided upon request to the first author of the paper.

Author contributions

DG and SL developed the ideas for the study. SW and SC conducted the numerical experiments. DG, CL, and SW analyzed and interpreted the results. DG prepared the paper. DG, CL and SW reviewed the paper.

Competing interests

The authors declare that they have no conflicts of interest.

Acknowledgements

Formatted: Header

Deleted: these can

Formatted: Font color: Black

Deleted: and the forecast model.

Deleted: fewer

Deleted: aspect,

Deleted: and environment.

Deleted: .

The work presented here is supported by NOAA NWS NGGPS R2O (Award number #NA15NWS468008). The NWS project is a collaborative effort from the University at Albany (Cheng-Hsuan Lu, Shih-Wei Wei, Sheng-Po Chen, and Dustin Grogan), NCEP/EMC (Robert Grumbine, Andrew Collard, Jun Wang, Partha Bhattacharjee, Bert Katz, Xu Li), and NESDIS/STAR (Quanhua Liu, Zhu Tong). The GDAS experiments were conducted at the University of Wisconsin-Madison Space Science and Engineering Center's Satellite Simulations and Data Assimilation Studies computer, or S4, cluster.

Formatted: Header

Deleted: UAlbany

Deleted: UW

References

Bercos-Hickey, E., Nathan, T.R., and Chen, S.-H.: Saharan dust and the African easterly jet–African easterly wave system: structure, location and energetics. Q. J. R. Meteorol. Soc., 143, 2797-2808, https://doi.org/10.1002/qj.3128, 2017.

Bercos-Hickey, E., Nathan, T.R., and Chen, S.-H.: On the Relationship between the African Easterly Jet, Saharan Mineral Dust Aerosols, and West African Precipitation, J. Clim., 143, 3533-3546, https://doi.org/10.1175/JCLI-D-18-0661.1, 2020

Benedetti A., and Coauthors: Status and future of numerical atmospheric aerosol prediction with a focus on data requirements, Atmos. Chem. Phys., 18, 10615-10643, https://doi.org/10.5194/acp-18-10615-2018, 2018.

Berry G.J., and Thorncroft C.D.: Case study of an intense African easterly wave. Mon. Wea. Rev. 123: 752-766, https://doi.org/10.1175/MWR2884.1, 2005

Brammer, A., and Thorncroft, C.D.: Variability and evolution of African easterly wave structures and their relationship with tropical cyclogenesis over the eastern Atlantic. Mon. Wea. Rev. 143, 4975-4995, https://doi.org/10.1175/MWR-D-15-0106.1, 2015.

Brammar A., and Thorncroft, C.D.: Spatial and temporal variability of the three-dimensional flow around African easterly waves, Mon. Wea. Rev., 145, 2879-2897, https://doi.org/10.1175/MWR-D-16-0454.1, 2017.

Bozzo, A., Remy, S., Benedetti, A., Fleming, J., Betchold, P., Rodwell, M.J., and Morcrette, J.-J.: Implementation of a CAMS-based aerosol climatology in the IFS. ECMWF Technical Memorandum, 801, Available at: https://www.ecmwf.int/en/elibrary/17771-radiation-numerical-weather-prediction (last access: 1 Feb 2021), 2017.

Burpee, R.W.: The origin and structure of easterly waves in the lower troposphere of North Africa. J. Atmos. Sci., 29, 77-90, https://doi.org/10.1175/1520-0469(1972)029<0077:TOASOE>2.0.CO;2, 1972.

Burpee, R.W.: Characteristics of North African Easterly Waves During the Summers of 1968 and 1969. J. Atmos. Sci., 31, 1556-1570, https://doi.org/10.1175/1520-0469(1974)031<1556:CONAEW>2.0.CO;2, 1974.

Carlson, T. N.: Some Remarks on African Disturbances and their Progress over the Tropical Atlantic. Mon. Wea. Rev., 97, No. 10, 716-726, https://doi.org/10.1175/1520-0493(1969)097<0716:SROADA>2.3.CO;2, 1969.

Chen, S.-H., Liu, Y.-C., Nathan, T.R., Davis, C., Torn, R., Sowa N., Cheng, C.-T., and Chen, J.-P.: Modeling the effects of dust-radiative forcing on the movement of Hurricane Helene (2006). Q. J. R. Meteorol. Soc, https://doi.org/10.1002/qj.2542, 2015.

Colarco, P., da Silva A., Chin M., Diehl T.: Online simulations of global aerosol distributions in the NASA GEOS-4 model and comparisons to satellite and ground-based aerosol optical depth. J. Geophys. Res. 115: D14207. https://doi.org/10.1029/2009JD012820, 2010

Cowie, S.M., Knippertz, P., and Marsham, J.H.: A climatology of dust emission events from northern Africa using long-term surface observations. Atmos. Chem. Phys., 14, 8579-8597, https://doi.org/10.5194/acp-14-8579-2014, 2014.

Formatted: Header

Formatted: First line: -2.4 ch

Moved (insertion) [3]

Formatted: Font: Times New Roman, 12 pt

Moved (insertion) [4]

Formatted

Moved (insertion) [5]

Formatted: First line: -2.4 ch

Deleted: Brammer,

Deleted: Predictability

Formatted

Deleted: a Nondeveloping Tropical Disturbance over

Formatted

Formatted: First line: -2.4 ch, Don't adjust space between Latin and Asian text, Don't adjust space between Asian text and numbers

Deleted: Eastern Atlantic.

Formatted

Formatted

Deleted: ., and

Formatted

Moved up [3]: J.

Deleted: Dunion: Observations

Formatted

Deleted: 146, 3079-3096

Formatted

Deleted: https://doi.org/10.1175/MWR-D-18-0065.1

Formatted

Deleted: 2018

Formatted

Formatted: First line: -2.4 ch

Deleted: Braun, S.A., Newman, P.A., and Heymsfield, G.M.: NASA's Hurricane and Severe Storm Sentinel (HS3) Investigation. Bull. Amer. Meteor. Soc., 2016, 2085-2102, https://doi.org/10.1175/BAMS-D-15-00186.1, 2016.¶

Formatted: First line: -2.4 ch

Deleted: Dunion, J.P., and Velden, C.S.: The Impact of the Saharan Air Layer on Atlantic Tropical Cyclone Activity

Cuesta, J., Marsham J.H., Parker D.H., Flamant C.: Dynamical mechanisms controlling the vertical redistribution of dust and the thermodynamic structure of the West Saharan atmospheric boundary layer during summer. Atmos. Sci. Let. 10: 34-42. https://doi.org/10.1002/asl.207, 2009.

Engelstaedter, S., and Washington R.: Atmospheric controls on the annual cycle of North African dust. J. Geophys. Res.-Atmos. 112: D03103, https://doi.org/10.1029/2006JD007195, 2007.

Grogan, D.F.P., Nathan, T.R., and Chen, S.-H.: Effect of Saharan dust on the linear dynamics of African easterly waves. J. Atmos. Sci. 73, 891-911, https://doi.org/10.1175/JAS-D-15-0143.1, 2016.

Grogan, D.F.P., Nathan, T.R., and Chen, S.-H.: Saharan dust and the nonlinear evolution of the African easterly jet–African easterly wave system. J. Atmos. Sci. 74, 24-47, https://doi.org/10.1175/JAS-D-16-0118.1, 2017.

Grogan, D.F.P. and Thorncroft, C.D.: The characteristics of African easterly waves coupled to Saharan mineral dust aerosols. Q. J. R. Meteorol. Soc. 2019, 1–17, https://doi.org/10.1002/qj.3483, 2019.

Grogan, D.F.P., Nathan, T.R., and Chen, S.-H.: Structural Changes in the African Easterly Jet and Its Role in Mediating the Effects of Saharan Dust on the Linear Dynamics of African Easterly Waves. J. Atmos. Sci. 76, 3359-3365, https://doi.org/10.1175/JAS-D-19-0104.1, 2019.

Han, Y., van Deist, P., Liu, Q., Weng, F., Yan, B., Treason, R., and Derber, J.: JCSDA community radiative transfer model (CRTM): Version 1. NOAA Technical Report NESDIS 122. Available at https://repository.library.noaa.gov/view/noaa/1157/noaa_1157_DS1.pdf (last access: 1 Feb 2021), 2006.

Hess, M.P., Koepke, P., and Shult, I.: Optical properties of aerosol and clouds: The software package OPAC. Bull. Amer Meteor. Soc., 79, 831-844, https://doi.org/10.1175/1520-0477(1998)079<0831:OPOAAC>2.0.CO;2, 1998.

Hsieh, J.-S., and Cook, K.H.: Generation of African easterly wave disturbances: relationship to the African easterly jet. Mon. Wea. Rev., 133, 1311-1327, https://doi.org/10.1175/MWR2916.1, 2005.

Jones, C., Mahowald, N., Luo, C. The role of easterly waves on African desert dust transport. J. Clim. 16: 3617-3628. https://doi.org/10.1175/1520-0442(2003)016<3617:TROEWO>2.0.CO;2, 2003.

Jones, C., Mahowald, N., and Luo, C.: Observational evidence of African desert dust intensification of easterly waves. Geophys. Res. Lett., 31, L17208, https://doi.org/10.1029/2004GL020107, 2004.

Jury, M.R. and Santiago, M.J.: Composite analysis of dust impacts on African easterly waves in the Moderate Resolution Imaging Spectrometer era. J. Geophys. Res., 115, D16213, https://doi.org/10.1029/2009JD013612, 2010.

Karyampudi, V.M., and Coauthors: Validation of the Saharan Dust Plume Conceptual Model Using Lidar, Meteosat, and ECMWF Data, Bull. Amer. Meteor. Soc., 1045-1076, https://doi.org/10.1175/1520-0477(1999)080<1045:VOTSDP>2.0.CO;2, 1999.

Formatted: Header

Moved down [6]: . Bull. Amer. Meteor. Soc.,

Deleted: 2004, 353-366, https://doi.org/10.1175/BAMS-85-3-353, 2004.

Formatted: First line: -2.4 ch

Deleted: Huneeus, N., Schulz, M., Balkanski, Y., Griesfeller, J., Prospero, M., Kinne, S., et al.: Global dust model intercomparison in AeroCom phase I

Moved up [4]: . Atmos. Chem. Phys.,

Formatted

Moved up [5]: Phys.,

Deleted: 11, 7781-7816, https://doi.org/10.5194/acp-11-7781-2011, 2011.

Formatted: First line: -2.4 ch

Moved (insertion) [6]

Kiladis, G.N., Thorncroft, C.D., and Hall, N.M.J.: Three-Dimensional Structure and Dynamics of African Easterly Waves. Part I: observations. J. Atmos. Sci. 63, 2212-2230, https://doi.org/10.1175/JAS3741.1, 2006.

Kim, J., Akella, S., da Silva, A.M., Todling, R., and McCarty, W.: Preliminary evaluation of influence of aerosols on the simulation of brightness temperature in NASA's Goddard Earth Observing System Atmospheric Data Assimilation System. Technical Report Series on Global Modeling and Data Assimilation, 49. Available at https://ntrs.nasa.gov/api/citations/20180001946/downloads/20180001946.pdf (last access: 1 Feb 2021), 2018.

Knippertz P, and Todd, M.C.: The central west Saharan dust hot spot and its relation to African easterly waves and extratropical disturbances. Geophys. Res. Lett. 115. https://doi.org/10.1029/2009D012819, 2010

Knippertz, P., and Todd, M.: Mineral dust aerosols over the Sahara: Meteorological controls on emission and transport and implications for modeling. Rev. Geophgys., 50, RG1007, https://doi.org/10.1029/2011RG000362, 2012.

Lorenc, A.C., and Rawlins, F.: Why Does 4D-Var Beat 3D-Var? Q. J. R. Meteorol. Soc. 2005, 131, 3247–3257, https://doi.org/10.1256/qj.05.85, 2005.

Lu, C.-H., and Coauthors: The implementation of NEMS GFS Aerosol Component (NGAC) Version 1.0 for global dust forecasting at NOAA/NCEP. Geosci. Model Dev., 9, 1906-1919, https://doi.org/10.5194/gmd-9-1905-2016, 2016.

Lu, C.-H., and Coauthors: The Aerosol Module in the Community Radiative Transfer Model (v2.2 and v2.3): accounting for aerosol transmittance effects on the radiance observation operator, et al. Geosci. Model Dev., under review, https://doi.org/10.5194/gmd-2021-145, 2021.

Hou, Y.-T., Moorhi, S., and Campana, K.: Parameterization of solar radiation transfer in the NCEP models. NCEP Office Note 441. Available at https://repository.library.noaa.gov/view/noaa/23085/noaa_23085_DS1.pdf (last access: 1 Feb 2021), 2002.

Mulcahey, J.-P., Walters, D.N., Bellouin, N., and Milton, S.F.: Impacts of increasing the aerosol complexity in the Met Office global numerical weather prediction model. Atmos. Chem. Phys., 14, 4749–4778, https://doi.org/10.5194/acp-14-4749-2014, 2014.

Nathan, T.R., Grogan, D.F.P., and Chen, S.-H.: Subcritical destabilization of African easterly waves by Saharan mineral dust. J. Atmos. Sci. 74, 1039-1055, https://doi.org/10.1175/JAS-D-16-0247.1, 2017.

Nathan, T.R., Grogan, D.F.P. and Chen. S.-H.: Saharan dust transport during the incipient growth phase of African easterly waves. Geosciences, 9, 388, https://doi.org/10.3390/geosciences9090388, 2019.

Norquist, D.C., Recker, E.R., and Reed, R.J.: The Energetics of African Wave Disturbances as observed During Phase III of GATE. Mon. Wea. Rev., 105, 334–342, https://doi.org/10.1175/1520-0493(1977)105<0334:TEOAWD>2.0.CO;2, 1977.

Paradis, D., Lafore, J.-P., Redelsperger, J.-L., and Balaji, V.: African easterly waves and convection. Part I: linear simulations. J. Atmos. Sci., 52, 1657-1679,

Formatted: Header

Formatted: First line: -2.4 ch

Formatted: First line: -2.4 ch

Formatted: Not Highlight

Formatted: Not Highlight

Formatted: First line: -2.4 ch

Deleted:

Formatted: First line: -2.4 ch

Deleted: Carlos

Formatted: Header

https://doi.org/10.1175/1520-0469(1995)052<1657:AEWACP>2.0.CO;2, 1995.

Pérez, C., Nickovic, S., Pejanovic, G., Baldasano, J.M., and Özsoy, E.: Interactive dust-radiation modeling: A step to improve weather forecasts. J. Geophys. Res. Lett., 111, D16206, https://doi.org/10.1029/2005JD006717, 2006.

Pytharoulis, I., and Thorncroft, C.D.: The low-level structure of African easterly waves in 1995. Mon. Wea. Rev., 127, 2266–2280, https://doi.org/10.1175/1520-0493(1999)127<2266:TLLSOA>2.0.CO;2, 1999.

Randles, C. A., and Coauthors: The MERRA-2 Aerosol Assimilation. NASA TM-2016-104606, Vol. 45, NASA Global Modeling and Assimilation Office, 132 pp, https://gmao.gsfc.nasa.gov/pubs/docs/Randles887.pdf, 2016.

Reed, R. J., Klinker, E., and Hollingsworth, A.: The structure and characteristics of African easterly wave disturbances as determined from the ECMWF operational analysis/forecast system. Meteorol. Atmos. Phys., 38, 22-33, https://doi.org/10.1007/BF01029944, 1988.

Reale, O., Lau, K.M., Kim, K.-Y., and Brin, E.: Atlantic Tropical Cyclogenetic Processes during SOP-3 NAMMA in the GEOS-5 Global Data Assimilation and Forecast System. J. Atmos. Sci., 66, 3563–3578, https://doi.org/10.1175/2009JAS3123.1, 2009.

Reale, O., and Lau, K.M.: Impact of an interactive aerosol on the African easterly jet in the NASA GOES-5 global forecasing system. Wea. Forecasting, 26, 504-519, https://doi.org/10.1175/WAF-D-10-05025.1, 2011.

Reale, O., Lau, K.M., da Silva, A.M., and Matsui, T.: Impact of assimilated and interactive aerosol on tropical cyclogenesis. Geophys. Res. Lett., 41, 3282–3288, https://doi.org/10.1002/2014GL059918, 2014.

Ross, R. S., and Krishnamurti, T.N.: Low-level African easterly wave activity and its relation to Atlantic tropical cyclogenesis in 2001. Mon. Wea. Rev., 135, 3950–3964, https://doi.org/10.1175/2007MWR1996.1, 2007.

Schwendike, J., and Jones, S.C.: Convection in an African Easterly Wave over West Africa and the eastern Atlantic: A model case study of Helene (2006). Q. J. R. Meteorol. Soc., 135, 364-396, https://doi.org/10.1002/qj.566, 2010.

Sokolik, I.: The spectral radiative signature of wind-blown mineral dust: Implications for remote sensing in the thermal IR region. Geophys. Res. Lett., 29, NO. 24, 2154, https://doi.org/10.1029/2002GL015910, 2002.

Thorncroft, C.D., and Hoskins, B.J.: An idealized study of African easterly waves. I: Linear theory. Q. J. R. Meteorol. Soc., 120, 953-982, https://doi.org/10.1002/qj.49712051809, 1994.

Thorncroft, C.D.: An idealized study of African easterly waves. III: More realistic basic states. Q. J. Roy. Meteorol. Soc. 121, 1589–1614. https://doi.org/10.1002/qj.49712152706, 1995.

Tegen, I., and Fung I.: Modeling of mineral dust in the atmosphere: Sources, transport, and optical thickness. J. Geophys. Res. 99, 22897-22914. https://doi.org/10.1029/94JD01928, 1994.

Wagner, R., Schepanski, K., Heinold, B., and Tegen, I.: Interannual variability in the Saharan dust source activation—toward understanding the differences between 2007 and 2008. J. Geophys Res. -Atmos 121, 4538–4562. https://doi.orx/10.1002/2015JD024302, 2017.

Formatted: First line: -2.4 ch

Formatted: First line: -2.4 ch

Formatted

Formatted: First line: -2.4 ch

Formatted: First line: -2.4 ch

Wang, J., and Coauthors: The implementation of NEMS GFS Aerosol Component (NGAC) Version 2.0 for global multispecies forecasting at NOAA/NCEP– Part 1: Model descriptions, Geosci. Model Dev., 11, 2315–2332, https://doi.org/10.5194/gmd-11-2315-2018, 2018.

Weaver, C.J., Joiner, J., and Ginoux, P.: Mineral aerosol contamination of TIROS Operational Vertical Sounder (TOVS) temperature and moisture retrievals. J. Geophys. Res. 2003, 108. https://doi.org/10.1029/2002JD002571, 2003.

Webb, N.P., and Strong, C.L.: Soil erodibility dynamics and its representation for wind erosion and dust emission models. Aeolian Res. 3, 165-179, https://doi.org/10.1016/j.aeolia.2011.03.002, 2011.

Westphal, D.L., Toon O.B., and Carlson, T.N.: A case study of mobilization and transport of Saharan dust. J. Atmos. Sci. 45, 2145-2175, https://doi.org/10.1175/1520-0469(1988)045<2145:ACSOMA>2.0.CO;2, 1988.

Wei, S.-W., Collard, A., Grumbine, R., Liu, Q., and Lu, C.-H.: Impacts of aerosols on meteorological assimilation: Aerosol impact on simulated brightness temperature and analysis fields. JCSDA Quarterly, 66, Spring 2020, https://doi.org/10.25923/4pt1-wx36, 2020.

Wei, S.-W., Lu, C.-H., Liu, Q., Collard, A., Zhu, T., Grogan, D.F.P., Li, X., Wang, J., Grumbine R., and Bhattacharjee, P.: The impact of aerosols on satellite radiance data assimilation using NCEP global data assimilation system. Atmosphere, 12(4), 432, https://doi.org/10.3390/atmos12040432, 2021.

Wilcox, E.M., Lau, K.M., and Kim, K.Y.: A northward shift of the North Atlantic Ocean Intertropical Convergence Zone in response to summertime Saharan dust outbreaks. Geophys. Res. Lett., 24, L04804, https://doi.org/10.1029/2009GL041774, 2010.

Formatted: Header

Formatted: First line: -2.4 ch

Deleted: et al.:

Formatted: First line: -2.4 ch

Deleted:

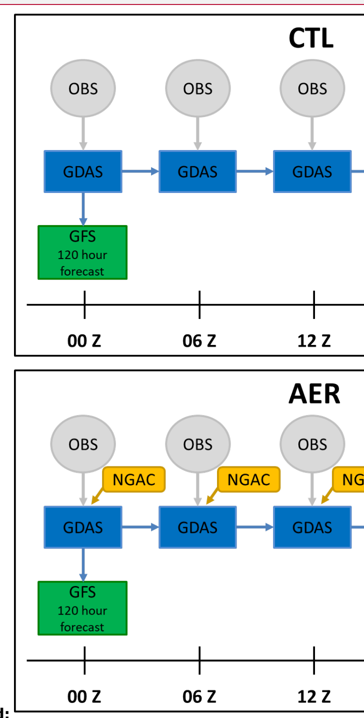

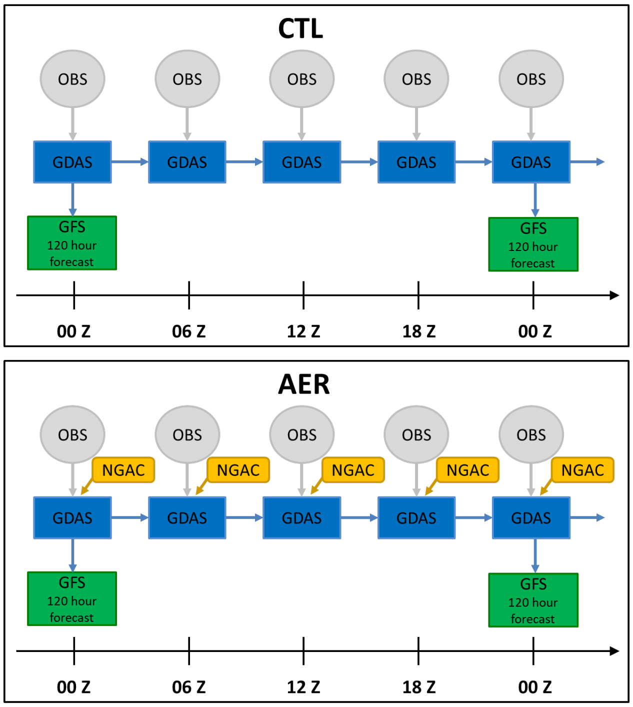

Figure 1. Schematic flow chart of the aerosol-blind (CTL) and aerosol-aware (AER) experiments in this study. See text for details.

Formatted: Header

Formatted: Font: 9 pt, Bold, Font color: Text 1

Formatted: Justified

Formatted: Font color: Text 1

Formatted: Font color: Text 1

Formatted: Indent: First line: 0", Line spacing: single

Deleted: for

Formatted: Font color: Text 1

Formatted: Font: 12 pt, Bold, Font color: Text 1

Formatted: Header

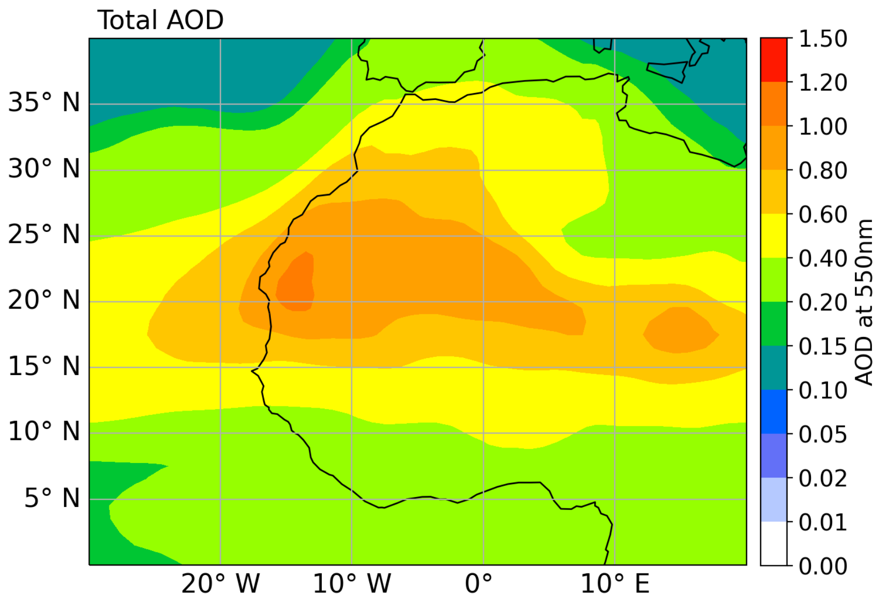

Figure 2. Total Aerosol Optical Depth (AOD) from the NGAC forecasts, averaged over August 1st-28th, 2017.

Deleted:

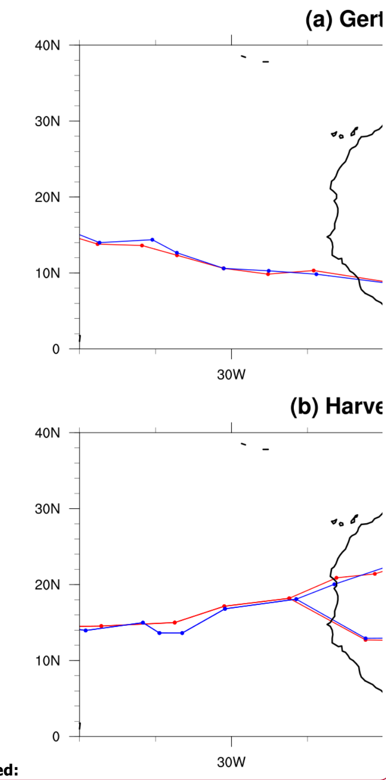

Formatted: Font color: Text 1

Formatted: Header

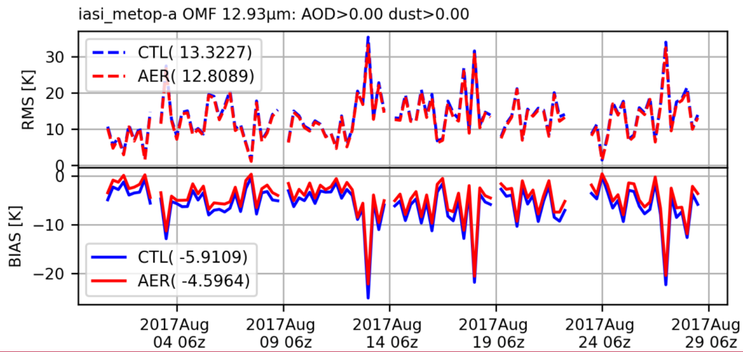

Figure 3. Statistics for the averaged observation-minus-forecast (OMF) infrared brightness temperatures (IR BT) (12.93µm) from the IASI hyperspectral sensor from CTL (red) and AER (blue). The timeseries includes all observations over the region (0-40°N, 20°E-30°W), irrespective of aerosol loading. The numbers in the legend are the mean statistics.

Formatted: Header

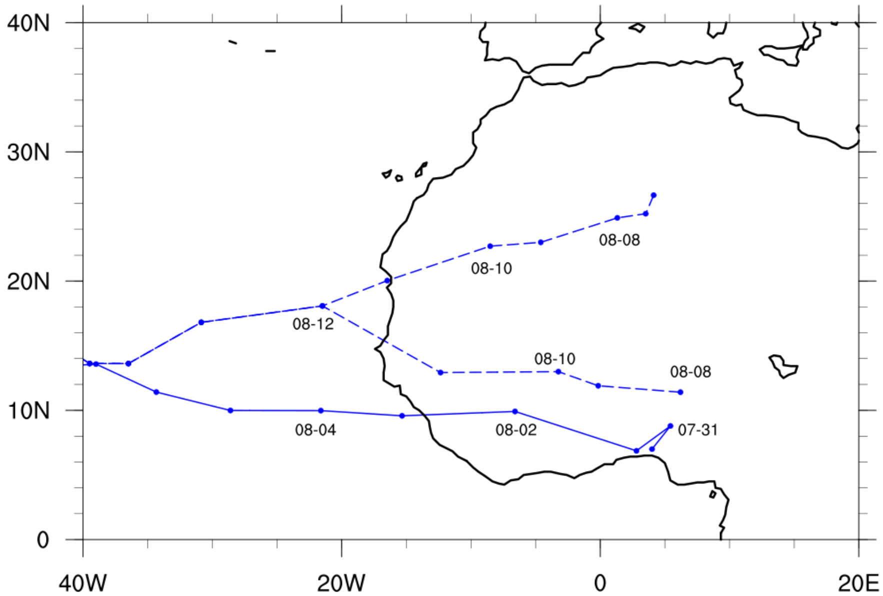

Figure 4. Daily locations (at 00 UTC) of the AEWs corresponding to Gert (solid) and Harvey (dashed) obtained by the tracking algorithm in the CTL run (time period: August, 2017).

Formatted: Line spacing: single

Deleted: from

Deleted: CTL (blue), AER (red).

Formatted: Font color: Text 1

Formatted: Indent: First line: 0", Line spacing: single

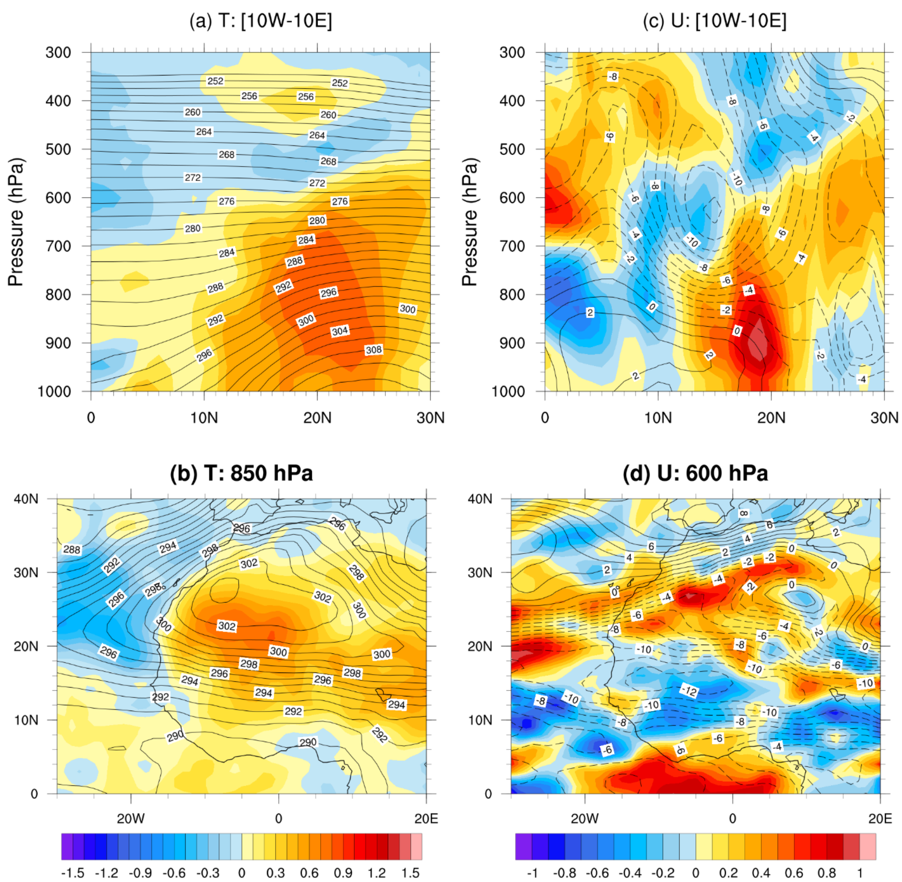

Figure 5. Vertical and horizontal cross sections of the CTL analysis (contours) and the AER – CTL analysis difference (colors) for (a, b) temperature, T, and (c, d) zonal wind, U. The vertical sections (top) are zonally-averaged from 10°W – 10°E, while horizontal sections (bottom) are taken at specified pressure levels. Contour/color units: (a,b) K and (c,d) ms^{-1}. The fields are time-averaged from August 1[st] – August 28[th], 2017.

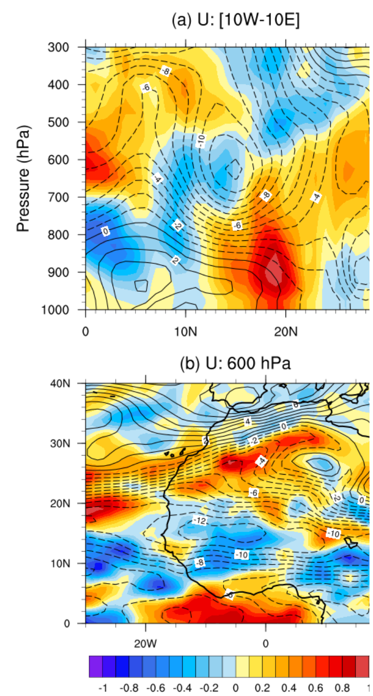

Deleted:

Deleted: 3. Horizontal

Deleted: vertical plots

Deleted: of the

Deleted: zonal-wind, U, and (c, d)

Deleted: ms^{-1}

Deleted: K

Deleted: computed

Formatted: Font color: Red

Formatted: Header

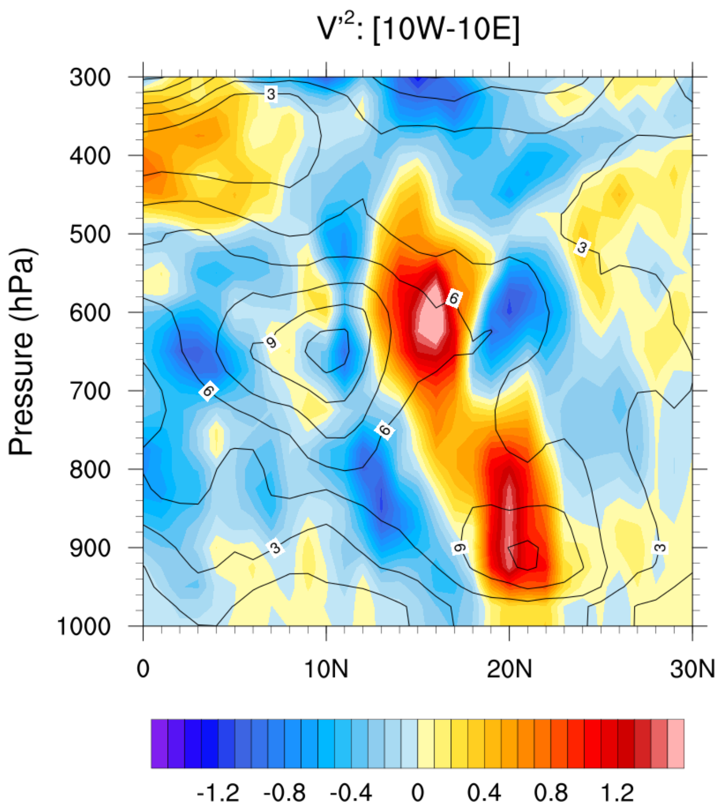

Deleted:

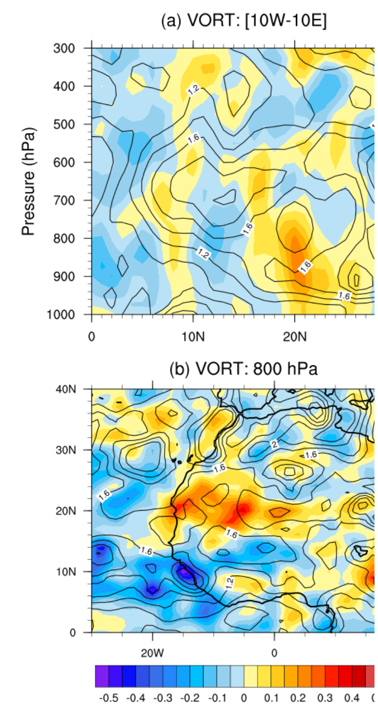

Figure 6. Time-averaged 2-6 day filtered meridional wind variances, v'^2, of the CTL analysis (contours) and the AER – CTL analysis difference (colors) zonally-averaged from 10°W – 10°E for August, 2017. Contour/color units: m^2s^{-2}.

Deleted: 4. As in Fig. 3, but for

Deleted: relative vorticity amplitude moduli, $VORT=(\zeta * \zeta)^{1/2}$, where ζ is

Deleted: relative vorticity.

Deleted: $x10^{-5}$ s^{-1}.

Formatted: Font color: Red

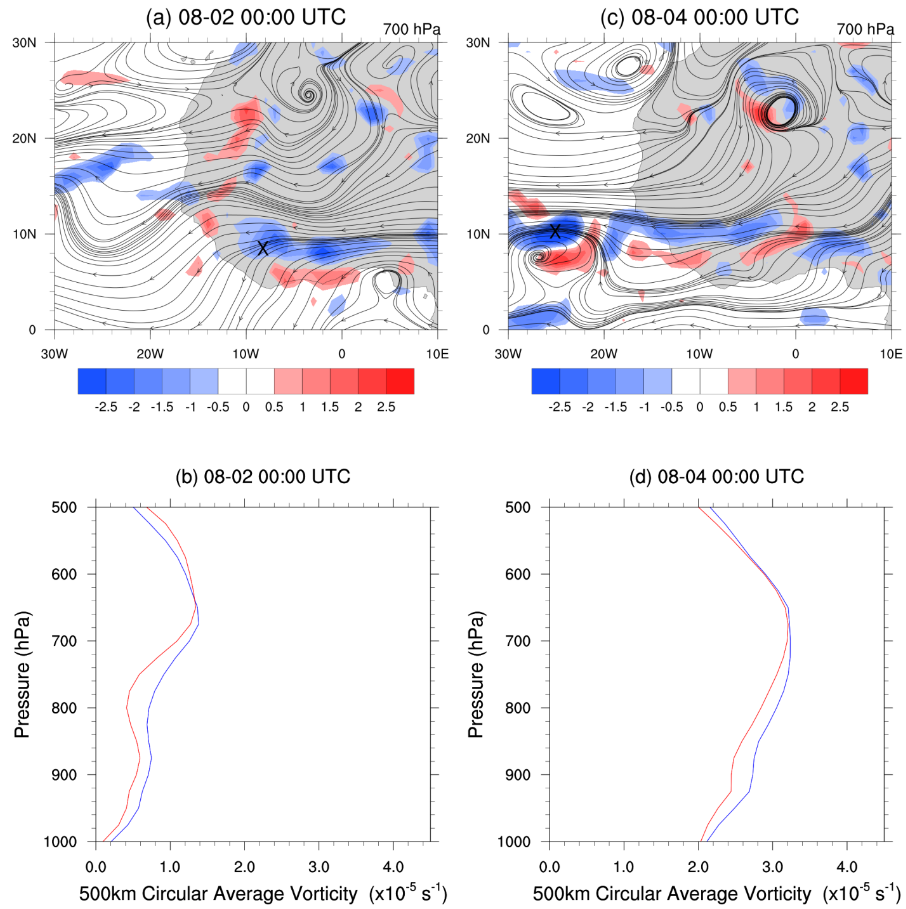

Figure 7. The evolution of the AEW associated with Gert on Aug 2nd (left) and Aug 4th (right). The top panels show the 700 hPa CTL streamlines (black) and the AER – CTL 700 hPa cyclonic vorticity differences (red/blue); the 'X' marks the wave's location from the tracking algorithm. The bottom panels show the circular average vorticity (radius 500 km) taken at the X's for CTL (blue) and AER (red).

Formatted: Header

Moved (insertion) [7]

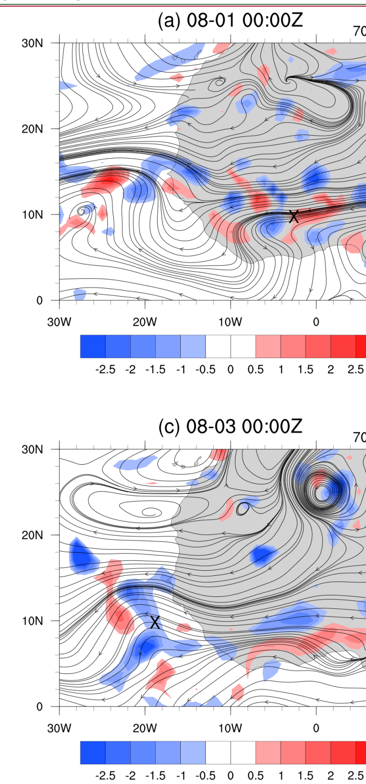

Deleted: ... [4]

Deleted: . The

Formatted: Font: Not Bold

Deleted: relative

Deleted: blues) from 00:00Z, Aug 1st – 4th. The

Deleted: storm

Deleted: To reduce clutter, the colors are only shown when the CTL flow is cyclonic (i.e., ζ >0) and the AER – CTL difference is more than ± 0.5x10^{-5}s^{-1}.¶ ... [5]

Deleted: for

Deleted: AEW associated with Gert

Deleted:) during August 1st – 4th. The circular averages are taken at the X's shown in Fig. 5, which are determined from the wave tracking algorithm.

Formatted: Font color: Red

Deleted: ----------Page Break----------¶ ... [6]

Moved up [7]: Figure 7.

Formatted: Font: Not Bold

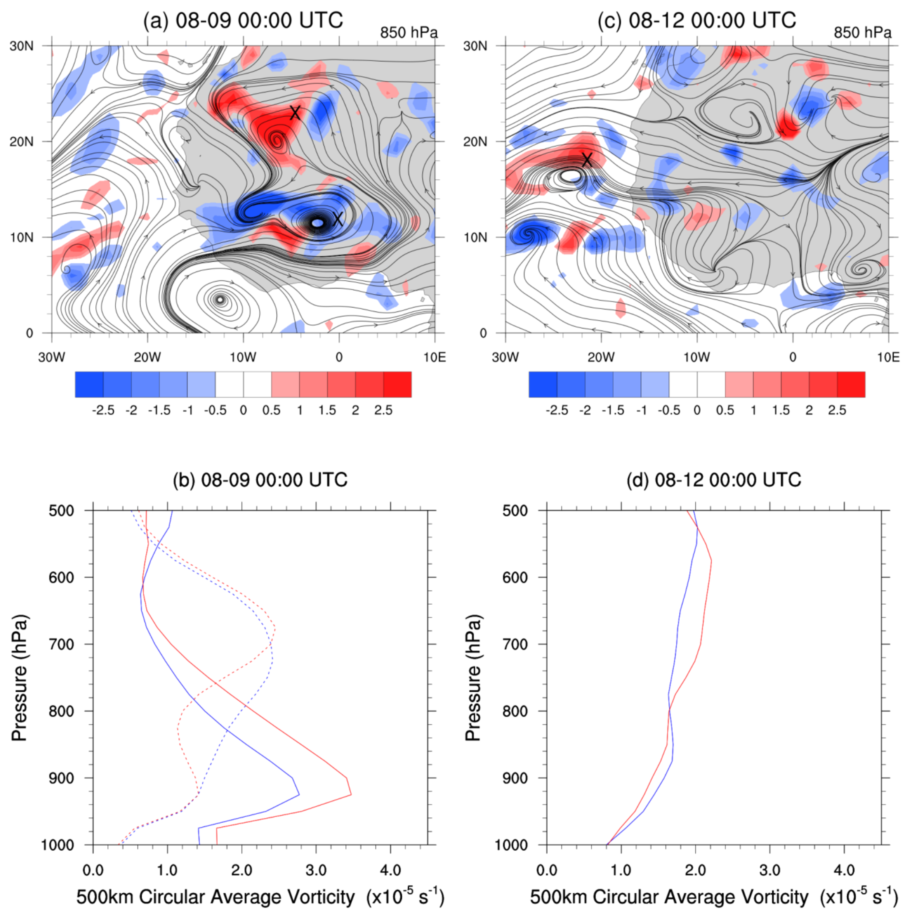

Figure 8. As in Fig. 7, but for the evolution of the AEW associated with Harvey on Aug 9th (left) and Aug 12th (right) The horizontal plots (top) show 850 hPa CTL streamlines and 850 hPa AER-CTL cyclonic vorticity differences, instead of 700 hPa, to better capture the two-circulation signal. Over Africa (b), we overlay the vertical vorticity structures of the northern (solid) and southern (dotted) circulation for CTL (blue) and AER (red).

Formatted: Header

Deleted: 5

Deleted: at 850 hPa. The date range is

Deleted: –

Deleted: .

Page Break

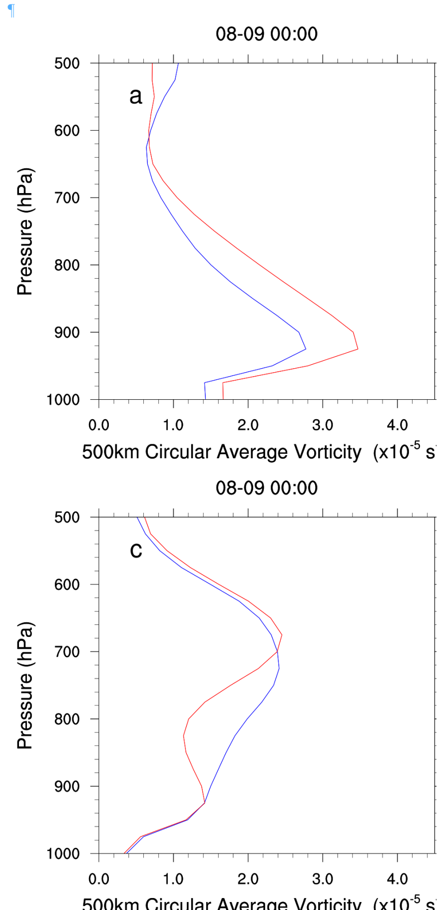

... [7]

Deleted: top

Deleted: bottom) circulations of the AEW associated with Harvey during August 9th – 10th.

Formatted: Font color: Red

Deleted:

Page Break

... [8]

Formatted: Header

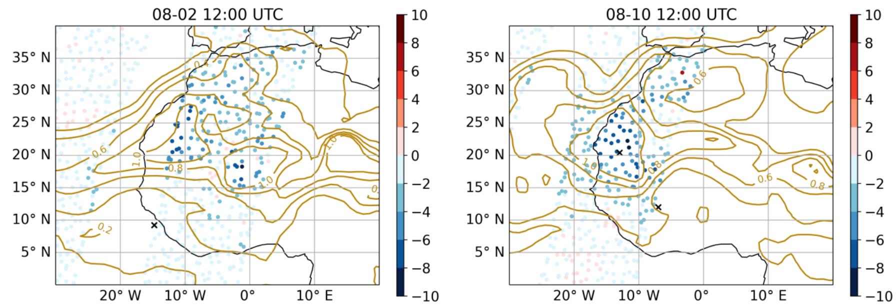

Figure 9. AER – CTL differences in simulated BT at 12.93µm from the IASI (colored circles) with the NGAC AOD (brown contours) on August 2^{nd}, 12:00 UTC (left) and Aug 10^{th}, 12:00 UTC (right). The X's mark the location of the wave centers for the AEW that developed Gert (left: 8°N,14°W) and Harvey (right: at 12°N,17°W and 20.5°N,13°W). Colorbar units: °K.

Deleted: 39µm

Deleted: on Aug 10^{th} 12:00Z

Deleted:).

Formatted: Font color: Red

Formatted: Header

Gert

Formatted Table

Initialization	1 day	2 day	3 day	4 day	5 day
July 31st	~~0.13~~	0.21	0.19	0.38	~~0.03~~
August 1st	0.17	0.27	0.25	~~0.10~~	~~0.08~~
August 2nd	0.19	~~0.04~~	0.24	~~0.10~~	~~0.08~~
August 3rd	~~0.06~~	0.20	0.23	~~0.09~~	1.02

Harvey

Formatted Table

Initialization	1 day	2 day	3 day	4 day	5 day
August 8th	0.23	~~0.05~~	0.23	0.32	0.27
August 9th	~~0.08~~	~~0.07~~	~~0.06~~	0.33	0.32
August 10th	0.35	0.32	0.17	0.31	0.49
August 11th	0.22	0.39	0.49	0.46	0.64

Table 1. RMSE relative differences in the 1000 – 500 hPa relative vorticity between the AER and CTL forecasts for the AEWs that developed Gert and Harvey. For each forecast day, the relative differences are calculated by taking (AER-CTL)/CTL of the RMSEs over the region following the AEWs (see text for more details). The green values indicate AER improved the forecast, while red values indicate AER degraded the forecast; crossed-out values were not significant to the 99% confidence interval. The staircase border in each case separates times when the waves are located onshore (upper left) and offshore (lower right).

Deleted: AEW

Page 10: [1] Deleted	Dustin G	10/15/21 10:09:00 AM

Page 16: [2] Deleted	Dustin G	10/15/21 10:09:00 AM

Page 16: [3] Deleted	Dustin G	10/15/21 10:09:00 AM

Page 31: [4] Deleted	Dustin G	10/15/21 10:09:00 AM

Page 31: [5] Deleted	Dustin G	10/15/21 10:09:00 AM

Page 31: [6] Deleted	Dustin G	10/15/21 10:09:00 AM

Page 32: [7] Deleted	Dustin G	10/15/21 10:09:00 AM

Page 32: [8] Deleted	Dustin G	10/15/21 10:09:00 AM